Ⓔ

Sensitivity Densities for Rotational Ground-Motion Measurements

by Andreas Fichtner and Heiner Igel

Abstract We derive and analyze sensitivity densities for two quantities derived from rotational ground-motion measurements: the rms (root-mean-square) amplitude A_ω of the rotation seismogram $\omega = \frac{1}{2} \nabla \times u$ and the apparent shear-wave speed $\beta_a = \frac{1}{2} A_v / A_\omega$, where A_v denotes the rms amplitude of the velocity seismogram. In the case of a plane S wave in a homogeneous and isotropic medium, β_a coincides with the true shear-wave speed β. Based on analytical and numerical examples, we demonstrate that the β_a kernels attain large absolute values only in the vicinity of the receiver but not in the vicinity of the source. This effect is pronounced in the case of both body S waves and surface waves (Love + Rayleigh). Moreover, the β_a kernels are dominated by the higher Fresnel zones while reaching only small absolute values in the first Fresnel zone. This implies (1) that measurements of β_a are to the first order independent of the Earth structure near the source, (2) that such measurements may be used for one-station local shear-wave speed tomography, and (3) that comparatively low-frequency signals can be used in order to invert for small-scale structures. The sensitivity densities corresponding to the rotation amplitude measurement A_ω resemble those for the velocity amplitude measurements A_v. It is, therefore, the combination of A_ω with A_v, and not one of them alone, that is likely to provide additional constraints on the Earth's structure near the receiver.

Online Material: Slices through 3D sensitivity kernels of the apparent shear-wave speed.

Introduction

In the course of the last decade direct measurements of seismically induced rotational ground motions have become feasible and reliable (e.g., Nigbor, 1994; Pancha *et al.*, 2000; Igel *et al.*, 2005, 2007). Theoretical seismologists (e.g., Aki and Richards, 2002) have argued for decades that in addition to the classical recording of translational motions, rotations should also be measured because only then is a complete description of the motion of a measurement point possible. Moreover, the mechanical characteristics of inertial seismometers necessitate knowledge of rotational ground motions. Seismometers are particularly sensitive to rotations about horizontal axes, that is, to tilt. This is one of the reasons why it is difficult to integrate acceleration or velocity recordings (e.g., Trifunac and Todorovska, 2001; Grazier 2005; Pillet and Virieux, 2007).

The analyses of broadband rotational and translational ground motions (Igel *et al.*, 2005, 2007) have indicated that even single station observations allow us to access information about the subsurface velocity structure, for example, through the derivation of phase velocities either in the time or frequency domain (Suryanto, 2006; Ferreira and Igel, 2008). This raises the question whether such joint observations can be used to further constrain the Earth structure. The primary goals of this article, therefore, are (1) to propose suitable measurements that can be derived from rotational and translational observations and (2) to illustrate their sensitivity to Earth's structure using the adjoint method.

Our focus will be on two quantities derived from the rotation seismogram $\omega = \frac{1}{2} \nabla \times \mathbf{u}$, where $\mathbf{u}$ denotes a synthetic or an observed displacement field: (1) the rotation amplitude $|\omega|$ and (2) the ratio $|\dot{\mathbf{u}}|/|\omega|$. The latter is a particularly attractive quantity in the context of structural inversion. Its unit is that of a velocity, suggesting that it yields very direct information about the Earth's wave speed structure. In fact, if we let $\mathbf{u}(\mathbf{x}^r, t)$ denote a displacement field recorded in a homogeneous and isotropic medium over time t at the location $\mathbf{x} = \mathbf{x}^r$, then the assumption that $\mathbf{u}(\mathbf{x}, t)$ is a plane shear-wave directly yields

$$\frac{|\dot{\mathbf{u}}(\mathbf{x}^r)|}{|\omega(\mathbf{x}^r)|} = 2\beta = 2\sqrt{\frac{\mu}{\rho}}. \tag{1}$$

In realistic Earth models, $\frac{1}{2} |\dot{\mathbf{u}}(\mathbf{x}^r, t)| / |\omega(\mathbf{x}^r, t)|$ is more appropriately referred to as apparent shear-wave speed. It generally depends on the types of waves considered and on their fre-

quency content, suggesting that different parts of the Earth can be sampled and that such measurements may be used to infer information about the Earth's structure.

The following sections are concerned with the derivation and analysis of sensitivity densities for rotation amplitudes and apparent shear-wave speed measurements, the emphasis being on the latter. Such sensitivity densities are an essential ingredient of linearized inversions and inversions based on gradient methods. Moreover, they provide general information on the possible origins of discrepancies between observed data and synthetics.

Prior to the actual derivation of sensitivity densities, we will introduce slightly modified definitions of the rotation amplitude and the apparent shear-wave speed. They are intended to better reflect the actual measurement process. The subsequent theoretical developments will result in a simple recipe for the computation of sensitivity densities. This recipe will then be applied to several special cases including *S* waves in a homogeneous medium, *S* waves in a radially symmetric Earth model, and surface waves recorded at regional distances. Throughout this article the sensitivity densities refer to the *S*-wave velocity β. Classical arrival time tomographies (e.g., Aki *et al.*, 1977 and many followers) usually favor the *S*-wave slowness β^{-1} as a parameter because its perturbations need not be linearized. In our case, however, the necessity to linearize perturbations of β does not arise as we will demonstrate later.

It should be noted that a relation similar to the one in equation (1) can be found by dividing acceleration amplitudes and rotation rate amplitudes. This may be more convenient in practice because rotation rates are the output of current rotation sensors based on optical principles (e.g., Nigbor, 1994; Takeo, 1998; Schreiber *et al.*, 2006). However, as we shall see later, acceleration measurements would lead to expressions for sensitivities involving fourth-order time derivatives of the seismic displacement field, which are numerically undesirable quantities.

Theory

Definition and Interpretation of the Apparent Shear-Wave Speed

So far, we loosely referred to the quantity $\frac{1}{2}|\dot{\mathbf{u}}(\mathbf{x}^r, t)|/|\omega(\mathbf{x}^r, t)|$ as the apparent shear-wave speed because it has the unit of a velocity and coincides with the shear-wave speed in the case of a homogeneous, unbounded, and isotropic medium. In practice, however, neither the pure determination of $|\omega|$ nor of the ratio $\frac{1}{2}|\dot{\mathbf{u}}(\mathbf{x}^r, t)|/|\omega(\mathbf{x}^r, t)|$ are particularly useful. Both filtering and averaging are often necessary operations that suppress the influence of noise and lead to more stable measurements. Moreover, one may wish to window the seismograms and isolate certain seismic phases or parts of a surface wave train, for example. In order to accommodate such processing steps in the formal measurement, we define the apparent shear-wave speed in terms

of the rms amplitudes of the filtered and windowed velocity and rotation signals

$$\beta_a(\mathbf{x}^r) := \frac{1}{2}\frac{A_v(\mathbf{x}^r)}{A_\omega(\mathbf{x}^r)}, \tag{2}$$

where A_v and A_ω are defined as

$$A_v := \sqrt{\int_{\mathbb{R}}[F * (W\mathbf{v})]^2 dt}, \qquad A_\omega := \sqrt{\int_{\mathbb{R}}[F * (W\omega)]^2 dt}. \tag{3}$$

The symbols *F* and *W* denote a convolution filter and a time window, respectively. Analogously, we shall from here on consider A_ω instead of $|\omega|$, noting that they are identical in the case that $W = F = 1$. One should strictly separate two aspects of β_a: (1) the interpretation of its numerical value and (2) its use as an observable for structural inverse problems. Interpreting β_a in terms of a true shear-wave speed is possible only when plane shear waves such as pure *S* or Love waves are considered. Then β_a may yield direct information about the subsurface structure. Whether the analyzed part of the seismogram is indeed a pure shear-wave or not is less important in the context of structural inverse problems. The apparent shear-wave speed is observable, regardless of its intuitive interpretation. Special care must be taken when $\omega = \mathbf{0}$ because the apparent shear-wave speed β_a is then not defined. One could in principle solve this problem by using β_a^{-1} instead, at least when $\mathbf{v} \neq \mathbf{0}$. Still, sensitivity kernels of β_a would not exist because A_ω is not differentiable at the point $\omega = \mathbf{0}$. In practice, ω may never truly vanish due to the presence of seismic noise. However, the values of β_a are not meaningful anyway when the rotation amplitude drops below the noise level.

Sensitivity Densities in the Context of the Adjoint Method

Our procedure for determining sensitivity kernels for synthetically computed apparent shear-wave speeds, β_a, is based on the adjoint method (e.g., Lions, 1968; Chavent *et al.*, 1975) because it leads to elegant expressions in an uncomplicated way and because its numerical implementation is straightforward. Alternatively, the sensitivity kernels could be derived using the Born approximation. In order to establish a consistent notation but also in the interest of completeness, we shall rederive or at least state some well-known results concerning the adjoint method in the context of elastic wave propagation. They may, for example, be found in one or the other form in Tarantola (1988), Tromp *et al.* (2005), or Fichtner *et al.* (2006).

We assume that $\mathbf{u}(\mathbf{x}, t)$ is an elastic displacement field, which is related to a set of model parameters $\mathbf{p}(\mathbf{x})$ and an external force density $\mathbf{f}(\mathbf{x}, t)$ via $\mathbf{L}(\mathbf{u}, \mathbf{p}) = \mathbf{f}$, where $\mathbf{L}$ represents the wave equation operator. More explicitly, one may write,

$$\mathbf{L}(\mathbf{u}, \mathbf{p}) = \rho(\mathbf{x})\partial_t^2 \mathbf{u}(\mathbf{x}, t) - \nabla \cdot \int_{-\infty}^{t} \mathbf{C}(\mathbf{x}, t - \tau){:}\nabla\mathbf{u}(\mathbf{x}, \tau)d\tau$$

$$= \mathbf{f}(\mathbf{x}, t). \tag{4}$$

The symbol : denotes the double scalar product, that is, $(\mathbf{C}{:}\nabla\mathbf{u})_{ij} = C_{ijkl}\partial_k u_l$. The model parameters $\mathbf{p}$ comprise the mass density ρ and the rate of relaxation tensor $\mathbf{C}$. We represent the process of measuring the wave field $\mathbf{u}$ or extracting information from it through an objective function $E(\mathbf{u})$, which we assume to be expressible in the form of a time integral $E(\mathbf{u}) = \int \epsilon(\mathbf{u})dt$ with an adequately chosen function ϵ. Given $\mathbf{u}$ as a function of time at the receiver position $\mathbf{x} = \mathbf{x}^r$, $E(\mathbf{u})$ may, for example, return cross-correlation time shifts (e.g., Luo and Schuster, 1991) or rms amplitudes (Dahlen and Baig, 2002) of seismic phases. The objective of the adjoint method is to provide an expression for the Fréchet kernel $\delta_p E$, that is, the volumetric density of the functional derivative of E with respect to the model parameters $\mathbf{p}$. In its most general form, this expression is

$$\delta_p E = \int_{\mathbb{R}} \mathbf{u}^\dagger \cdot \partial_p \mathbf{L}(\mathbf{u}, \mathbf{p})\, dt, \tag{5}$$

where $\partial_p \mathbf{L}$ denotes the partial derivative of the operator $\mathbf{L}$ with respect to the model parameters. The adjoint field $\mathbf{u}^\dagger$ is defined through the adjoint wave equation

$$\mathbf{L}^\dagger(\mathbf{u}^\dagger, \mathbf{p}) = \rho(\mathbf{x})\partial_t^2 \mathbf{u}^\dagger(\mathbf{x}, t)$$

$$- \nabla \cdot \int_{-\infty}^{t} \mathbf{C}(\mathbf{x}, \tau - t){:}\nabla\mathbf{u}^\dagger(\mathbf{x}, \tau)\, d\tau$$

$$= -\partial_u \epsilon(t)\delta(\mathbf{x} - \mathbf{x}^r) \tag{6}$$

and its subsidiary conditions. Note that (6) is still of the wave equation type. The external force density is proportional to the derivative of ϵ with respect to the observed wave field $\mathbf{u}$, and it acts at the receiver location $\mathbf{x}^r$. In the case of an isotropic and nondissipative medium described in terms of the mass density ρ and the Lamé parameters μ and λ, the three Fréchet kernels are

$$\delta_\rho E = -\int_{\mathbb{R}} \partial_t \mathbf{u}^\dagger \cdot \partial_t \mathbf{u}\, dt,$$

$$\delta_\mu E = \int_{\mathbb{R}} (\nabla\mathbf{u}^\dagger){:}[(\nabla\mathbf{u}) + (\nabla\mathbf{u})^T]\, dt, \tag{7}$$

$$\delta_\lambda E = \int_{\mathbb{R}} (\nabla \cdot \mathbf{u}^\dagger)(\nabla \cdot \mathbf{u})\, dt.$$

Expressions for Fréchet kernels with respect to the S-wave speed β or the P-wave speed α can then be derived from equation (7). A special case of outstanding importance arises when $E(\mathbf{u})$ is equal to the i component of the displacement field, $u_i(\mathbf{x}^r, \tau)$, that is, when $\epsilon(\mathbf{u}) = \delta(t - \tau)\mathbf{e}_i \cdot \mathbf{u}(\mathbf{x}^r, t)$. The right-hand side of the adjoint equation (6) then becomes $-\mathbf{e}_i\delta(t - \tau)\delta(\mathbf{x} - \mathbf{x}^r)$, implying that the corresponding ad-

joint field $\mathbf{u}^\dagger$ is the negative adjoint to Green's function with a source location $\mathbf{x}^r$ and a source time τ, that is, $\mathbf{u}^\dagger(\mathbf{x}, t) = -\mathbf{g}_i^\dagger(\mathbf{x}^r, \tau; \mathbf{x}, t)$. Therefore, we have

$$\delta_p u_i(\mathbf{x}^r, \tau) = -\int_{\mathbb{R}} \mathbf{g}_i^\dagger(\mathbf{x}^r, \tau; \mathbf{x}, t) \cdot \partial_p \mathbf{L}[\mathbf{u}(\mathbf{x}, t)]dt. \tag{8}$$

We now proceed with our actual problem, which is the derivation of Fréchet kernels for apparent S-wave speed measurements. The definition in equation (2) directly yields

$$\frac{1}{\beta_a}\delta_\beta \beta_a = \delta_\beta \ln \beta_a = \frac{1}{A_v}\delta_\beta A_v - \frac{1}{A_\omega}\delta_\beta A_\omega$$

$$= \delta_\beta \ln A_v - \delta_\beta \ln A_\omega. \tag{9}$$

Letting β_a, A_v, and A_ω play the roles of objective functions, we can rewrite equation (9) using the adjoint method terminology,

$$\delta_\beta \ln \beta_a = \int_{\mathbb{R}} \psi^v \cdot \partial_\beta \mathbf{L}(\mathbf{u}, \mathbf{p})dt - \int_{\mathbb{R}} \psi^\omega \cdot \partial_\beta \mathbf{L}(\mathbf{u}, \mathbf{p})dt$$

$$=: \int_{\mathbb{R}} \psi^{\beta_a} \cdot \partial_\beta \mathbf{L}(\mathbf{u}, \mathbf{p})dt, \tag{10}$$

where ψ^v and ψ^ω are the adjoint fields for A_v and A_ω, respectively. For convenience, we incorporated the scaling factors A_v^{-1} and A_ω^{-1} into the definitions of the adjoint fields. The key element of equation (10) is the difference of the adjoint fields $\psi^{\beta_a} := \psi^v - \psi^\omega$. We will demonstrate in a later section that this difference; and therefore, the sensitivity kernel $\delta_\beta \ln \beta_a$, is large in the vicinity of the receiver but small in the source region.

Before, however, we will derive general expressions for the adjoint fields ψ^v and ψ^ω. The analysis will be kept general in the sense that we will not consider derivatives with respect to one particular parameter but with respect to any possible parameter. The numerical examples will then focus on sensitivity densities with respect to the shear-wave speed β.

The Adjoint Field for Velocity Amplitude Measurements

The relative functional derivative of A_v with respect to the model parameters $\mathbf{p}$ denoted by $A_v^{-1}D_p A_v$ is

$$\frac{1}{A_v}D_p A_v = \frac{1}{A_v^2}\int_{\mathbb{R}} [F * (W\mathbf{v})] \cdot [F * (WD_p\mathbf{v})]\, dt$$

$$= \frac{1}{A_v^2}\int_{\mathbb{R}} (\mathfrak{F}\dot{u}_i)D_p\dot{u}_i\, dt. \tag{11}$$

For notational brevity we defined the composite filter $\mathfrak{F}$ in equation (11) as

$(\mathfrak{F}\dot{u}_i)(\mathbf{x}^r, t)$

$$:= W(t) \int_{-\infty}^{\infty} \left[\int_{-\infty}^{\infty} F(\tau_2 - \tau_1) W(\tau_1) \dot{u}_i(\mathbf{x}^r, \tau_1) d\tau_1 \right]$$
$$\times F(\tau_2 - t) d\tau_2. \tag{12}$$

The term in square brackets is the convolution filter $F(t)$ applied to the windowed velocity seismogram $(W\dot{u}_i)(t)$. In the frequency domain, the action of $F(t)$ corresponds to a multiplication with $\hat{F}(\omega) = |\hat{F}(\omega)|e^{i\phi}$. This operation is then followed by a convolution with $F(-t)$, that is, by a multiplication with $|\hat{F}(\omega)|e^{-i\phi}$ in the frequency domain. Hence, the double integral acts as a zero phase filter on $W\dot{u}_i$. This ensures that the second application of the window W in front of the double integral in equation (12) indeed affects the signal of interest. Equation (11) can be rewritten in terms of sensitivity densities,

$$\frac{1}{A_v} D_p A_v = \int_{G \subset \mathbb{R}^3} \mathbf{p}' \frac{1}{A_v} \delta_p A_v dG$$
$$= \frac{1}{A_v^2} \int_{\mathbb{R}} (\mathfrak{F}\dot{u}_i) D_p \dot{u}_i dt$$
$$= \int_{G \subset \mathbb{R}^3} \mathbf{p}' \frac{1}{A_v^2} \int_{\mathbb{R}} (\mathfrak{F}\dot{u}_i) \delta_p \dot{u}_i dt dG, \tag{13}$$

where $\mathbf{p}'$ is the differentiation direction. The symbols G and dG denote the computational domain and the corresponding volume element, respectively. Using the expression for $\delta_p u_i$ (equation 8) we now deduce that the sensitivity density $A_v^{-1} \delta_p A_v = \delta_p \ln A_v$ can be written as

$$\delta_p \ln A_v = -\frac{1}{A_v^2} \int_{\mathbb{R}^2} (\mathfrak{F}\dot{u}_i)(\mathbf{x}^r, t) \partial_t \mathbf{g}_i^\dagger(\mathbf{x}^r, t; \mathbf{x}, t')$$
$$\cdot \partial_p \mathbf{L}[\mathbf{u}(\mathbf{x}, t')] dt' dt$$
$$= \frac{1}{A_v^2} \int_{\mathbb{R}^2} \partial_t (\mathfrak{F}\dot{u}_i)(\mathbf{x}^r, t) \mathbf{g}_i^\dagger(\mathbf{x}^r, t; \mathbf{x}, t')$$
$$\cdot \partial_p \mathbf{L}[\mathbf{u}(\mathbf{x}, t')] dt' dt. \tag{14}$$

Then defining the adjoint field ψ^v to be

$$\psi^v(\mathbf{x}, t') := \frac{1}{A_v^2} \int_{\mathbb{R}} \partial_t (\mathfrak{F}\dot{u}_i)(\mathbf{x}^r, t) \mathbf{g}_i^\dagger(\mathbf{x}^r, t; \mathbf{x}, t') dt \tag{15}$$

gives the desired canonical form

$$\delta_p \ln A_v = \int_{\mathbb{R}} \psi^v(\mathbf{x}, t') \cdot \partial_p \mathbf{L}[\mathbf{u}(\mathbf{x}, t')] dt'. \tag{16}$$

Equation (15) implies that ψ^v can equally be obtained as the solution of the adjoint equation $\mathbf{L}^\dagger(\psi^v, \mathbf{p}) = \mathbf{f}^v$, where the adjoint source $\mathbf{f}^v$ is given by

$$\mathbf{f}^v(\mathbf{x}, t') = \frac{1}{A_v^2} \partial_t (\mathfrak{F}\dot{u}_i)(\mathbf{x}^r, t') \delta(\mathbf{x} - \mathbf{x}^r). \tag{17}$$

The Adjoint Field for Rotation Amplitude Measurements

We now repeat the steps that led to the expression of the adjoint source for velocity amplitude measurements ψ^v in order to obtain the corresponding expression for rotation amplitude measurements. Differentiating the windowed and filtered rms amplitudes of the rotational ground motion $A_\omega = \sqrt{\int_{\mathbb{R}} [F * (W\omega)]^2 dt}$ with respect to the model parameters $\mathbf{p}$ yields

$$\frac{1}{A_\omega} D_p A_\omega = \frac{1}{A_\omega^2} \int_{\mathbb{R}} [F * (W\omega)] \cdot [F * (WD_p\omega)] dt$$
$$= \frac{1}{A_\omega^2} \int_{\mathbb{R}} (\mathfrak{F}\omega_i) D_p \omega_i dt. \tag{18}$$

Because ω and $\mathbf{u}$ are related through $\omega_i(\mathbf{x}^r, t) = \frac{1}{2} \epsilon_{ijk} \frac{\partial}{\partial x_j^r} u_k(\mathbf{x}^r, t)$, we have

$$\delta_p \omega_i(\mathbf{x}^r, t) = \frac{1}{2} \epsilon_{ijk} \frac{\partial}{\partial x_j^r} \delta_p u_k(\mathbf{x}^r, t)$$
$$= -\frac{1}{2} \epsilon_{ijk} \int_{\mathbb{R}} \frac{\partial}{\partial x_j^r} \mathbf{g}_k^\dagger(\mathbf{x}^r, t; \mathbf{x}, t') \cdot \partial_p \mathbf{L}[\mathbf{u}(\mathbf{x}, t')] dt'. \tag{19}$$

We then substitute equation (19) into the expression for $A_\omega^{-1} \delta_p A_\omega = \delta_p \ln A_\omega$, which follows from equation (18), and find

$$\delta_p \ln A_\omega = -\frac{1}{2A_\omega^2} \epsilon_{ijk} \int_{\mathbb{R}} \int_{\mathbb{R}} (\mathfrak{F}\omega_i)(\mathbf{x}^r, t) \frac{\partial}{\partial x_j^r} \mathbf{g}_k^\dagger(\mathbf{x}^r, t; \mathbf{x}, t')$$
$$\cdot \partial_p \mathbf{L}[\mathbf{u}(\mathbf{x}, t')] dt' dt. \tag{20}$$

The canonical form

$$\delta_p \ln A_\omega = \int_{\mathbb{R}} \psi^\omega(\mathbf{x}, t') \cdot \partial_p \mathbf{L}[\mathbf{u}(\mathbf{x}, t')] dt' \tag{21}$$

can then be obtained by defining the adjoint field ψ^ω as follows:

$$\psi^\omega(\mathbf{x}, t') := -\frac{1}{2A_\omega^2} \epsilon_{ijk} \int_{\mathbb{R}} (\mathfrak{F}\omega_i)(\mathbf{x}^r, t) \frac{\partial}{\partial x_j^r} \mathbf{g}_k^\dagger(\mathbf{x}^r, t; \mathbf{x}, t') dt. \tag{22}$$

It is again possible to compute the adjoint field ψ^ω by solving an adjoint equation of the form $\mathbf{L}^\dagger(\psi^\omega, \mathbf{p}) = \mathbf{f}^\omega$. From equation (22) we deduce that the components f_k^ω of the adjoint source $\mathbf{f}^\omega$ are

$$f_k^\omega(\mathbf{x}, t') = \frac{1}{2A_\omega^2} \epsilon_{ijk}(\mathfrak{F}\omega_i)(\mathbf{x}^r, t') \frac{\partial}{\partial x_j} \delta(\mathbf{x} - \mathbf{x}^r). \tag{23}$$

It is interesting to note that $\mathbf{f}^\omega$ can be written in terms of a moment density $\mathbf{m}$, that is, in the form $\mathbf{f}^\omega = -\nabla \cdot \mathbf{m}$. The components m_{kj} of the moment density are

$$m_{kj} = -\frac{1}{2A_\omega^2} \epsilon_{ijk}(\mathfrak{F}\omega_i)(\mathbf{x}^r, t')\delta(\mathbf{x} - \mathbf{x}^r). \qquad (24)$$

Unlike realistic moment densities corresponding, for example, to slip on a fault plane, $\mathbf{m}$ is antisymmetric. This highlights the fact that the adjoint field is a purely mathematical construction that is potentially unphysical. It follows from the antisymmetry of $\mathbf{m}$ that the adjoint source $\mathbf{f}^\omega$ does not radiate far-field P waves. Therefore, the interaction of the forward field $\mathbf{u}$ and the adjoint field ψ^ω (see equation 21) is primarily limited to the interaction of S waves and the near-field terms.

Case Studies

Homogeneous, Unbounded, and Isotropic Medium

If one wishes to derive some general properties of the β_a kernels, then there are only two options: one may simplify the forward problem using, for example, ray theory while keeping the Earth model realistic (e.g., Yomogida, 1992; Dahlen and Baig, 2002), or one may simplify the Earth model while using exact solutions of the wave equation. Here we shall adopt a variant of the latter approach by considering a homogeneous, unbounded, and isotropic medium. While this is unrealistic, it still allows us to deduce some fundamental characteristics of the β_a kernels, which will reappear in more complicated cases that we will treat numerically. We assume that the incident wave is an S wave. Because the adjoint P wave propagates at the P velocity α, it interacts with the forward S wave only inside a sphere around the receiver. The radius of this sphere is $R_p = \lambda_p \alpha/(\alpha - \beta)$, where λ_p is the wavelength of the P wave. The adjoint S wave, however, interacts with the forward S wave throughout the entire volume that is filled by the Fresnel zones. Thus, it contributes significantly more to the derivatives of A_v and A_ω than the adjoint P wave. Accepting that the Fréchet kernels will not be exact in the sphere of radius R_p around the receiver; we will neglect the adjoint P wave. Also, the near-field terms of the adjoint wave field are disregarded because they only contribute in the immediate vicinity of the receiver. Both the adjoint P wave and the near-field terms will automatically be included in the numerical examples that we present in the following sections. The n component of the S wave contribution of the adjoint Green's function $\mathbf{g}_i^\dagger(\mathbf{x}^r, t; \mathbf{x}, t')$ is

$$(\mathbf{g}_i^\dagger)_n(\mathbf{x}^r, t; \mathbf{x}, t') = \frac{\delta_{in} - \gamma_i^r \gamma_n^r}{4\pi\rho\beta^2|\mathbf{x} - \mathbf{x}^r|}\delta(t' - t + |\mathbf{x} - \mathbf{x}^r|/\beta)$$

$$(25)$$

with $\gamma_i^r := (x_i - x_i^r)/|\mathbf{x} - \mathbf{x}^r|$. Substituting equation (25) into equation (15) yields an expression for the adjoint wavefield ψ^v

$$\psi_n^v(\mathbf{x}, t') = \frac{\delta_{in} - \gamma_i^r(\mathbf{x})\gamma_n^r(\mathbf{x})}{4\pi\rho\beta^2 A_v^2|\mathbf{x} - \mathbf{x}^r|}\partial_{t'}(\mathfrak{F}\dot{u}_i)(\mathbf{x}^r, t' + |\mathbf{x} - \mathbf{x}_r|/\beta).$$

$$(26)$$

The corresponding expression for ψ_n^ω is

$$\psi_n^\omega(\mathbf{x}, t') = \frac{\epsilon_{ijn}\gamma_j^r}{8\pi\rho\beta^3 A_\omega^2|\mathbf{x} - \mathbf{x}^r|}\partial_{t'}(\mathfrak{F}\omega_i)(\mathbf{x}^r, t' + |\mathbf{x} - \mathbf{x}^r|/\beta),$$

$$(27)$$

where we used $\frac{\partial}{\partial x_j}|\mathbf{x} - \mathbf{x}^r| = \gamma_j^r$ and $\epsilon_{ijk}\gamma_j^r\gamma_k^r = 0$. Under the assumption that the receiver at $\mathbf{x} = \mathbf{x}^r$ is far away from the source at $\mathbf{x} = \mathbf{0}$, we obtain the following expression for ω_i:

$$\omega_i(\mathbf{x}^r, t' + |\mathbf{x} - \mathbf{x}^r|/\beta) = -\frac{1}{2}\epsilon_{ipq}$$

$$\times \frac{\gamma_p(\mathbf{x}^r)}{\beta}\dot{u}_q(\mathbf{x}^r, t' + |\mathbf{x} - \mathbf{x}^r|/\beta),$$

$$(28)$$

where $\gamma_p(\mathbf{x}) := x_p/|\mathbf{x}|$ is the direction cosine measured from the source located at the coordinate origin. Combining equations (27) and (28) yields

$$\psi_n^\omega(\mathbf{x}, t') = -\frac{\epsilon_{ijn}\epsilon_{ipq}\gamma_j^r(\mathbf{x})\gamma_p(\mathbf{x}^r)}{16\pi\rho\beta^4 A_\omega^2|\mathbf{x} - \mathbf{x}^r|}\partial_{t'}(\mathfrak{F}\dot{u}_q)$$

$$\times (\mathbf{x}^r, t' + |\mathbf{x} - \mathbf{x}^r|/\beta)$$

$$= \frac{\gamma_i^r(\mathbf{x})\gamma_n(\mathbf{x}^r) - \gamma_i^r(\mathbf{x})\gamma_j(\mathbf{x}^r)\delta_{ni}}{4\pi\rho\beta^2 A_\omega^2|\mathbf{x} - \mathbf{x}^r|}\partial_{t'}(\mathfrak{F}\dot{u}_i)$$

$$\times (\mathbf{x}^r, t' + |\mathbf{x} - \mathbf{x}^r|/\beta). \qquad (29)$$

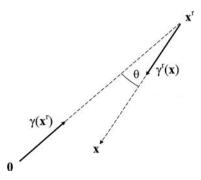The adjoint field ψ^{β_a} is equal to the difference $\psi^v - \psi^\omega$

$$\psi_n^{\beta_a}(\mathbf{x}, t')$$

$$= \frac{\delta_{in} - \gamma_i^r(\mathbf{x})\gamma_n^r(\mathbf{x}) - \gamma_i^r(\mathbf{x})\gamma_n(\mathbf{x}^r) + \gamma_j^r(\mathbf{x})\gamma_j(\mathbf{x}^r)\delta_{ni}}{4\pi\rho\beta^2 A_v^2|\mathbf{x} - \mathbf{x}^r|}$$

$$\times \partial_{t'}(\mathfrak{F}\dot{u}_i)(\mathbf{x}^r, t' + |\mathbf{x} - \mathbf{x}_r|/\beta). \qquad (30)$$

The radiation pattern contribution to the amplitude of the adjoint field ψ^{β_a} can be estimated using some basic geometrical relations that are illustrated in Figure 1:

$$|\psi_n^{\beta_a}| \propto |\delta_{in}[1 + \gamma_j^r(\mathbf{x})\gamma_j(\mathbf{x}^r)]\ddot{u}_i$$

$$- [\gamma_i^r(\mathbf{x})\gamma_n^r(\mathbf{x}) + \gamma_i^r(\mathbf{x})\gamma_n(\mathbf{x}^r)]\ddot{u}_i|$$

$$\leq |1 - \cos\theta||\ddot{\mathbf{u}}| + |\sin\theta||\gamma_n^r(\mathbf{x}) + \gamma_n(\mathbf{x}^r)||\ddot{\mathbf{u}}|$$

$$= |1 - \cos\theta||\ddot{\mathbf{u}}| + \sqrt{2}|\sin\theta|\sqrt{1 - \cos\theta}|\ddot{\mathbf{u}}| \doteqdot \frac{3}{2}\theta^2|\ddot{\mathbf{u}}|.$$

$$(31)$$

The symbol $\doteqdot$ denotes correct to second order in θ'. According to equation (31), the adjoint field does not radiate towards the source. Moreover, in the vicinity of the source, that is, for small $|\mathbf{x}|$, we find $\theta \leq |\mathbf{x}|/|\mathbf{x} - \mathbf{x}^r|$; and therefore,

$$|\psi^{\beta_a}(\mathbf{x}, t')| \leq \frac{3|\mathbf{x}|^2|\ddot{\mathbf{u}}|}{8\pi\rho\beta^2 A_v^2|\mathbf{x} - \mathbf{x}^r|^2}. \qquad (32)$$

Figure 1. Source-receiver geometry. The source is located at the origin 0, and the receiver is at $\mathbf{x}^r$. The point where the kernel is computed is denoted by $\mathbf{x}$.

Equation (32) implies that the adjoint field tends to zero as we approach the source. The convergence is quadratic in $|\mathbf{x}|$. Because $|\mathbf{u}|$ itself is proportional to $1/|\mathbf{x}|$, it follows from equation (5) that the sensitivity kernel $\delta_p \ln \beta_a$ is proportional to $|\mathbf{x}|$, where p denotes *any* model parameter, possibly β. In symbols

$$\delta_p \ln \beta_a \propto |\mathbf{x}| \rightarrow \lim_{|\mathbf{x}| \to 0} \delta_p \ln \beta_a = 0. \qquad (33)$$

The sensitivity kernel $\delta_p \ln \beta_a$ vanishes as we approach the source. A consequence of equation (33) is that the apparent shear-wave speed β_a is only weakly affected by an Earth structure near the source. Sensitivity densities of β_a with respect to any model parameter, for example, β, Q, or the (anisotropic) elastic tensor components c_{ijkl}, exhibit this behavior at least in this simple medium. This is a clear contrast to sensitivity kernels of other quantities such as cross-correlation time shifts (Marquering *et al.*, 1999; Dahlen *et al.*, 2000), rms amplitudes (Dahlen *et al.*, 2002), or rotation amplitudes. The mathematical reason for this behavior of the apparent shear-wave speed kernels is that the kernels $\delta_p \ln A_v$ and $\delta_p \ln A_\omega$ become increasingly similar as the distance from the source decreases. Note that this statement strictly holds only when all components of ω are taken into account. Some of the components may be naturally zero, for example, when Love waves in a stratified medium are analyzed. Disregarding, however, nonzero components of ω will generally lead to sensitivity kernels that do have significant contributions further away from the receiver.

Note that the result from equation (33) is still valid when both the adjoint P wave and the adjoint near-field terms are included. Their contribution to the Fréchet kernels is confined to a small region around the receiver. In the following section the kernels will be computed numerically in a more realistic Earth model. The adjoint P wave and near-field terms will automatically be included. This will allow us to study the structure of the Fréchet kernels near the receiver. We will, moreover, be able to assess whether the kernels still vanish as we approch the source.

S Waves from a Deep Earthquake Recorded at Regional Distances

As we pass from an oversimplified to a more realistic Earth model, analytic solutions become unavailable. In what follows, the solutions of the wave equation will, therefore, be computed numerically (Oeser *et al.*, 2006) using a spectral-element method described in Fichtner and Igel (2008).
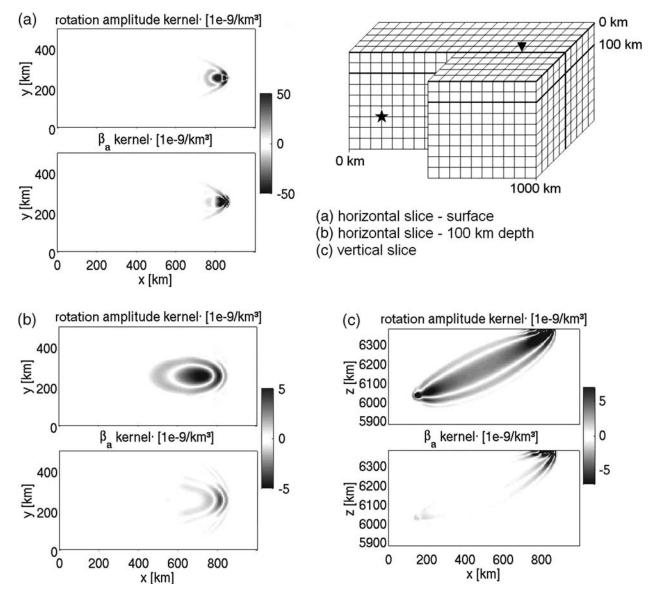
The kernel gallery that we shall compile in the course of the next sections is intended to serve multiple purposes. First, it aims at providing physical intuition, which is the foundation of any application of the sensitivity kernels to inverse problems, for example. Secondly, we shall confirm some of the results that we found for the case of the homogeneous, isotropic, and unbounded medium.

In our first numerical example, we consider S waves originating from a 300 km deep source that are recorded at an epicentral distance of 650 km. The source time function is a low-pass filtered Heaviside function with a cutoff period of 10 sec, and the Earth model is AK135 (Kennett *et al.*, 1995). Slices through the rotation amplitude kernels $\delta_\beta \ln A_\omega$ and the apparent shear-wave speed kernels $\delta_\beta \ln \beta_a$ are shown in Figure 2. (Ⓔ Color versions of all figures are available in the electronic edition of *BSSA*.) Both sensitivity kernels attain comparatively large absolute values in the immediate vicinity of the receiver (Fig. 2a). While their shapes, though not their actual values, are similar at the surface, they become increasingly dissimilar with increasing distance from the receiver (Fig. 2b). The vertical slices in Figure 2c give the best general impression of the kernel characteristics. They confirm that the apparent shear speed sensitivity is small, in fact, as good as negligible, in the vicinity of the source.

The velocity amplitude kernels $\delta_\beta \ln A_v$ are not displayed because they resemble the rotation amplitude kernels to an extent that makes them hard to distinguish visually. This implies that velocity amplitude and rotation amplitude measurements yield similar information about the Earth's structure. It is the combination of A_ω and A_v that potentially provides additional constraints in the vicinity of the receiver. The width of all sensitivity kernels depends strongly on the frequency content of the analyzed waves. In general, lower frequency signals generate broader kernels while the kernels corresponding to higher frequency signals are slimmer. This effect is clearly visible in Figure 3 where the cutoff period is chosen to be 20 sec instead of 10 sec as in Figure 2. The broadening with respect to the higher frequency kernels is most significant near the surface.

Surface Waves from a Shallow Source

The geometric setup of our next example is similar to the previous one except that the source is now located at a depth of 10 km. Therefore, the synthetic seismograms are dominated by large-amplitude surface waves (Fig. 4). We set the moment tensor components to $M_{xy} = M_{xz} = 1 \cdot 10^{19}$ Nm and $M_{xx} = M_{yy} = M_{zz} = M_{yz} = 0$. Consequently, both
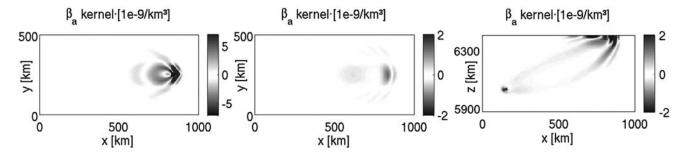
Figure 2.   Slices through the rotation amplitude kernels $\delta_\beta \ln A_\omega$ and the apparent shear-wave speed kernels $\delta_\beta \ln \beta_a$ in the 1D Earth model AK135 (Kennett *et al.*, 1995). The source is located at the depth of 300 km (star), and the direct S wave is recorded at an epicentral distance of 650 km (triangle). The cutoff period of the signal is 10 sec. (a) Horizontal slices at the surface through the rotation amplitude kernel $\delta_\beta \ln A_\omega$ (top) and the apparent shear-wave speed kernel $\delta_\beta \ln A_\omega$ (below). Both kernels attain their largest values directly at the receiver position. (b) As (a) but at the depth of 100 km. (c) Vertical slices through $\delta_\beta \ln A_\omega$ (top) and $\delta_\beta \ln \beta_a$ (below). The absolute values of the β_a kernel decrease away from the receiver, so that β_a measurements are most sensitive to the Earth structure near the receiver and less sensitive to structures at greater distances, at least correct to the first order. (Ⓔ A color version of this figure is available in the electronic edition of *BSSA*.)

Love and Rayleigh waves are recorded along the x axis (see Fig. 2 for the geometry of the model). In realistic applications this will almost always be the case, first, because of lateral heterogeneities and second, because of source localization and orientation errors.

This has immediate consequences on the interpretability of the ratio $\beta_a = \frac{1}{2} A_v / A_\omega$. If we analyzed only a single-mode Love wave, then β_a would equal the phase velocity corresponding to that particular Love wave mode. However, this statement does not hold when Rayleigh waves are involved as well. Already in the classical single-layer model, β_a be-

comes a complicated function that is generally different from β. We omit the analytic formula for β_a in the single-layer model also because it is of little practical relevance. Instead, we compute β_a for the complete surface wave train and with sliding windows for a station at an epicentral distance of $\Delta = 1500$ km in our numerical model:

The left column of Figure 4 shows dispersed Love waves (y component) arriving around 350 sec followed by the Rayleigh waves on the x and z components. The corresponding rotational motion recordings are plotted in the middle column. There is no rotational motion in x direction due

Figure 3. Slices through the apparent shear-wave speed kernel $\delta_\beta \ln \beta_a$ for a cutoff period of 20 sec. Left: Horizontal slice at the surface. The geometry of the kernel is similar to the 10 sec version in Figure 2a but has a significantly wider lateral extension. Center: Horizontal slice at the depth of 100 km. The geometry of the kernel differs from the one of the 10 sec kernel. Right: Vertical slice parallel to the source-receiver line. The kernel is concentrated near the receiver, whereas its absolute values decrease toward the source. (Ⓔ A color version of this figure is available in the electronic edition of *BSSA*.)

to our particular choice of the source orientation. We now determine apparent shear-wave speeds in two different ways: First, we compute β_a for the complete surface wave train between 350 and 550 sec. The result, $\beta_a = 2830$ km/sec, is represented by the bold lines in the right column of Figure 4. Second, we compute apparent shear-wave speeds for the seismograms windowed by sliding tapers that are 10 sec, 25 sec, and 50 sec wide. (Examples with real data can be found in Igel *et al.*, 2005, 2007.) The resulting apparent shear-wave speeds, $\beta_a^{(10)}$, $\beta_a^{(25)}$, and $\beta_a^{(50)}$, correspond to the thin lines in the right column of Figure 4. From 350 to 400 sec, the seismograms are dominated by the Love waves. Consequently, the time-dependent $\beta_a^{(10)}$, $\beta_a^{(25)}$ and $\beta_a^{(50)}$ attain values that are close to the phase velocity of a 20 sec Love wave propagating along continental paths, that is, ≈ 4 km/sec. Between 450 and 500 sec, the Rayleigh wave becomes dominant, and one might intuitively expect that the time-dependent apparent shear-wave speeds should increase because Rayleigh waves do not only depend on β but also on

the much larger *P*-wave speed α. This, however, is not the case. Instead, $\beta_a^{(10)}$, $\beta_a^{(25)}$, and $\beta_a^{(50)}$, collectively, drop below the mean value of 2830 km/sec mainly because ω_y attains comparatively large values after 450 sec.

One possible explanation for this observation is the dispersion of the surface wave train. Due to the dispersion, the sliding windows always sample a certain frequency band $(\omega_0 - \Delta\omega, \omega_0 + \Delta\omega)$. Making the plane wave approximation together with the assumption that the *z* component of the displacement for $\omega \in [\omega_0 - \Delta\omega, \omega_0 + \Delta\omega]$ can be represented as

$$u_z(x, t) = \int_{\omega_0 - \Delta\omega}^{\omega_0 + \Delta\omega} \cos(\omega t - k(\omega)x)d\omega, \qquad (34)$$

gives the well-known result (e.g., Lay and Wallace, 1995)

$$u_z(x, t) = \Delta\omega \, \text{sinc}[\Delta\omega(t - k_0'x)/2] \cos(\omega_0 t - k_0 x). \quad (35)$$
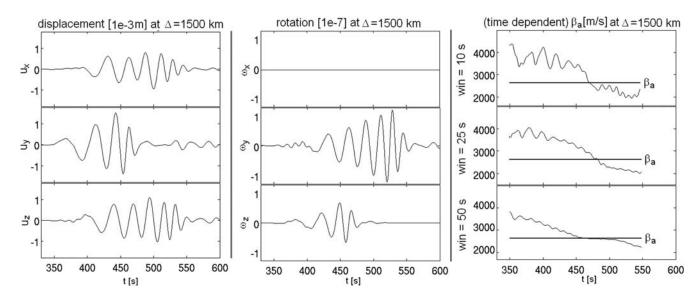

Figure 4. Left: Surface wave displacements at $\Delta = 1500$ km. Center: Rotational motion at $\Delta = 1500$ km. Right: Time-dependent ratio $\frac{1}{2}|\mathbf{v}(\mathbf{x}^r, t)|/|\omega(\mathbf{x}^r, t)|$ computed with sliding windows that are 10 sec, 25 sec, and 50 sec wide. The bold vertical line indicates the value of β_a for the complete surface wave train.

This equation is valid when the linear term of the Taylor expansion $k(\omega) = k(\omega_0) + k'(\omega_0)(\omega - \omega_0) + \ldots = k_0 + k_0'(\omega - \omega_0) + \ldots$ is dominant. The y component of the rotational motion, ω_y, is proportional to $\partial_x u_z$ for which we find

$$\partial_x u_z(x, t) = -\frac{1}{2}\Delta\omega^2 k_0' \mathrm{sinc}'[\Delta\omega(t - k_0'x)]\cos(\omega_0 t - k_0 x)$$
$$+ \Delta\omega k_0 \mathrm{sinc}[\Delta\omega(t - k_0'x)]\sin(\omega_0 t - k_0 x). \tag{36}$$

The first summand in equation (36) is proportional to $k_0' = c_g(\omega_0)^{-1}$, where c_g denotes the group velocity. This summand is mostly small because of $\Delta\omega^2$, but it can nevertheless have a contribution when c_g is comparable to $c_0\Delta\omega/\omega_0$, that is, when

$$c_g(\omega_0) \approx c(\omega_0)\frac{\Delta\omega}{\omega_0}. \tag{37}$$
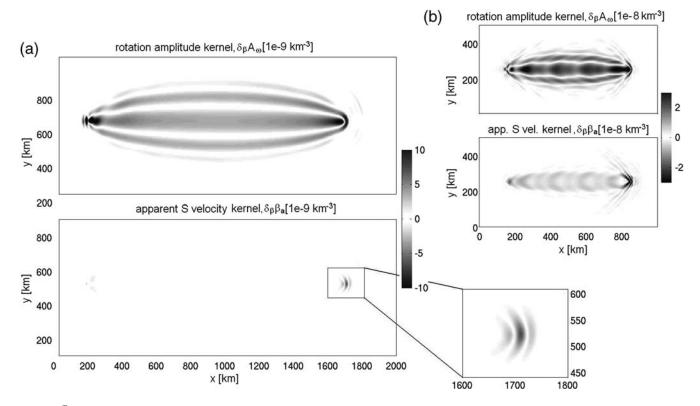
This can be the case under the following circumstances: (1) The band width $\Delta\omega$ is comparable to the center frequency, ω_0 and/or (2) the group velocity is small. In our particular example, both factors play a role because the high amplitudes of ω_y appear in the latest arrivals (small c_g) for which the frequency is relatively high.

Despite the fact that β_a, for the entire wave train or for sliding windows, is not always directly interpretable as

S-wave speed, it is a physically valid measurement. In general, this measurement, that is, the particular value that it yields, depends on the Earth's structure. Therefore, we can compute the corresponding sensitivity kernels. Some of the results are displayed in Figure 5.

Part (a) of Figure 5 shows horizontal slices through the rotation amplitude kernel $\delta_\beta \ln A_\omega$ and through the corresponding apparent shear velocity kernel $\delta_\beta \ln \beta_a$ for the station at an epicentral distance of $\Delta = 1500$ km. While $\delta_\beta \ln A_\omega$ fills the space between source and receiver, the apparent S-velocity kernel is restricted to the immediate vicinity of the receiver. This result is similar to the one obtained for body S waves, and it corroborates the hypothesis that this phenomenon is independent of the type of seismic waves that one uses for the analysis.

Note that the epicentral distance of 1500 km is much larger than the one chosen for the body S waves in the S Waves from a Deep Earthquake Recorded at Regional Distances section (650 km). In fact, reducing the epicentral distance in the surface wave case to 650 km leads to substantial contributions to the β_a kernel between source and receiver as can be seen in Figure 5b. A rigorous and quantitative analysis of this observation is beyond the scope of this article. Nevertheless, it can be explained qualitatively. The behavior of the kernel $\delta_\beta \ln \beta_a$ depends on the characteristics of the adjoint wave field $\psi^{\beta_a} = \psi^v - \psi^\mu$ and therefore on the differences

Figure 5. (a) Horizontal slices at 10 km depth through the rotation amplitude kernel $\delta_\beta \ln A_\omega$ (top) and the corresponding apparent shear speed kernel $\delta_\beta \ln \beta_a$ (below). The epicentral distance is $\Delta = 1500$ km. (b) The same as (a) but for a shorter epicentral distance of $\Delta = 650$ km. (Ⓔ A color version of this figure is available in the electronic edition of *BSSA*.)

between ψ^v and ψ^ω. In the case of body waves, the difference $\psi^v - \psi^\omega$ decays as $1/r$ away from the receiver. However, when surface waves are considered, the geometric spreading of the adjoint field away from the receiver is proportional to $1/\sqrt{r}$. Therefore, differences between ψ^v and ψ^ω are carried much further into the source region. As Figure 5 indicates, this effect can be compensated for by increasing the epicentral distance.

The characteristics of $\delta_\beta \ln \beta_a$ at a greater depth are illustrated in Figure 6, which shows vertical slices through the source-receiver line. The images have different shading scales in order to emphasize the relative amplitudes of the kernel in different regions. Contributions along the source-receiver path are almost entirely absent. The sensitivity of β_a to the S-wave speed β is restricted to the immediate vicinity of the receiver and to depths of less than 50 km.

Outlook: Possible Setups of Inverse Problems Using β_a Measurements

The ultimate purpose of the β_a and A_ω kernels is to facilitate the solution of structural inverse problems in which the apparent shear-wave speed or the rotation amplitude serve as observables. While the analysis and the solution of such an inverse problem are beyond the scope of this article, we still want to outline three of its possible formulations in order to highlight how the sensitivity kernels may be used in practice. Our focus will be on apparent shear speed measurements. The corresponding expressions for rotation amplitude measurements are easily obtained by replacing β_a by A_ω.

Formulation 1: Linearized Inverse Problem

It is, in principle, possible to use observations of β_a in the context of a linearized inverse problem that is conceptually similar to the one encountered in classical ray tomography (e.g., Aki *et al.*, 1977). The components d_i of the n-dimensional data vector $\mathbf{d}$ are defined as the relative differences between the observations $\beta_{a,i}^{(0)}$ and their corresponding synthetic values $\beta_{a,i}$, that is,

$$d_i := (\beta_{a,i} - \beta_{a,i}^{(0)})/\beta_{a,i}, \quad i = 1, \ldots, n. \tag{38}$$

Different index values i may, for example, denote various events, seismic phases, stations, dominant frequencies, or combinations of them. Under the assumption that $\beta_{a,i}$ is able to linearize around the parameter p, not necessarily the S-wave speed β, we may write,
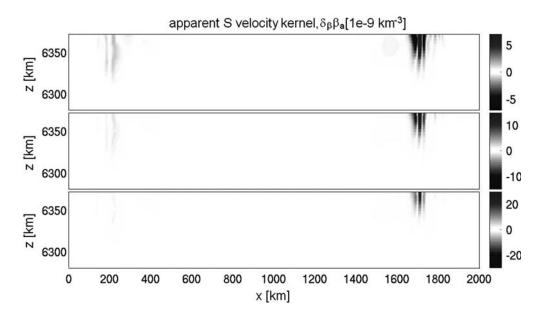
$$\begin{aligned} d_i &= (\beta_{a,i} - \beta_{a,i}^{(0)})/\beta_{a,i} \\ &= [\beta_{a,i}(p) - \beta_{a,i}(p^{(0)})]/\beta_{a,i}(p) \\ &= [\beta_{a,i}(p) - \beta_{a,i}(p + \delta p)]/\beta_{a,i}(p) \\ &\doteq - \int_G (\delta_p \ln \beta_{a,i}) \delta p \, dG, \end{aligned} \tag{39}$$

where $p^{(0)}$ denotes the true parameter and G the spatial domain where the wave field and the kernel $\delta_p \ln \beta_{a,i}$ are defined. Even though p is usually an infinite-dimensional function, such as a shear-wave speed or density distribution, it needs to be expressed in terms of a finite-dimensional basis in order to make the problem computationally tractable. By letting $h_k(\mathbf{x})$, $k = 1, \ldots, m$ denote the basis elements, we can express $p(\mathbf{x})$ and $\delta p(\mathbf{x})$ as

Figure 6. Vertical slices through $\delta_\beta \ln \beta_a$ along the source-receiver line. The image is plotted with different shading scales in order to emphasize the different amplitudes of the kernel in the source and receiver regions. (Ⓔ A color version of this figure is available in the electronic edition of *BSSA*.)

$$p(\mathbf{x}) = \sum_{j=1}^{m} p_j h_j(\mathbf{x}), \qquad \delta p(\mathbf{x}) = \sum_{j=1}^{m} \delta p_j h_j(\mathbf{x}). \quad (40)$$

Equation (39) then transforms to

$$d_i = \sum_{j=1}^{m} \delta p_j \left[-\int_G (\delta_p \ln \beta_{a,i}) h_j dG \right], \quad (41)$$

or in matrix notation

$$\mathbf{d} = \mathbf{A}\delta\mathbf{p}, \qquad A_{ij} := -\int_G (\delta_p \ln \beta_{a,i}) h_j dG. \quad (42)$$

This linear tomographic system, or a regularized version of it, may then be solved using standard iterative techniques. (See Nolet [1993] for an overview.)

Formulation 2: Nonlinear Inverse Problem and Gradient Methods

In the case that $\beta_{a,i}$ is not sufficiently able to linearize well, it is preferable to view the inverse problem as an iterative minimization of a nonlinear misfit function $E(\beta_{a,i})$. One may, for example, choose the quadratic function

$$E(\beta_{a,i}) = \frac{1}{2} \sum_{i=1}^{n} (\beta_{a,i} - \beta_{a,i}^{(0)})^2. \quad (43)$$

The gradient of E with respect to the model parameters p_j required by the method of steepest descent and its variants, is then given by

$$\frac{dE}{dp_j} = \sum_{i=1}^{n} (\beta_{a,i} - \beta_{a,i}^{(0)}) \frac{d\beta_{a,i}}{dp_j}, \quad (44)$$

where the gradient of $\beta_{a,i}$ is expressible through the kernel $\delta_p \beta_{a,i}$:

$$\frac{d\beta_{a,i}}{dp_j} = \int_G h_j \delta_p \beta_{a,i} \, dG = -\beta_{a,i} A_{ij} \quad (45)$$
$$\text{(no summation over } i\text{).}$$

Formulation 3: Nonlinear Inverse Problem and Monte Carlo Minimization

Monte Carlo methods offer an alternative to the minimization of the misfit E by means of gradient methods, especially when the problem is highly nonlinear. Because Monte Carlo methods generally do not require information on the gradient of E, the sensitivity kernels are not used directly. They may, however, be of indirect use because they potentially provide information on where random perturbations of a test model are most effective. In that sense, gradient infor-

mation may be used for the benefit of a more economic random model generation.

Discussion

We have demonstrated that sensitivity densities for apparent shear speed measurements become negligibly small in regions that are far from the receiver. This property is reminiscent of SKS splitting kernels (Sieminski *et al.*, 2008), and it suggests that β_a may be used for the estimation of local Earth structure. In addition to being comparatively small near the source, $\delta_\beta \ln \beta_a$ generally possesses another characteristic feature, namely that contributions in the higher Fresnel zones are enhanced at the expense of suppressed contributions in the first Fresnel zones. [We employ the term, Fresnel zone, in the interest of greater clarity even though the considered signals are usually quasiperiod and not strictly periodic.] There are several implications arising from this phenomenon: (1) Higher Fresnel zones are generally thinner than the first Fresnel zone. It follows that for a given dominant frequency ν, β_a measurements yield more information on small-scale structures than measurements of the rms amplitudes A_v and A_ω or measurements of cross-correlation time shifts (e.g., Dahlen *et al.*, 2000). In the inverse problem context this means that one may, and probably must, generally work with comparatively low frequencies when β_a measurements are used as data. Otherwise, the β_a measurement will be sensitive to very small-scale structure that one may not be able to resolve. (2) The shape of $\delta_\beta \ln \beta_a$ is rather susceptible to waveform changes. This is not the case for kernels that attain large values in the first Fresnel zone. Rotation and velocity amplitude kernels are two examples. Consequently, small changes in the Earth model will lead to changes in the β_a kernels that are larger than in the A_v or A_ω kernels. Carefully incorporating already known 3D Earth structure into the computation of the synthetic seismograms is therefore essential when β_a measurements are to be used for structural inversions. (3) As mentioned in the Outlook: Possible Setups of Inverse Problems section, sensitivity densities are often not used directly. Instead, they are multiplied by a basis function h_j and integrated over the computational domain (see equation 45). This procedure is meaningful only when the scale of the principal features of the sensitivity densities is comparable to the characteristic length scale of the basis function. Hence, if we wish to exploit the comparatively large values of $\delta_\beta \ln \beta_a$ in the receiver region, then the characteristic length scale of h_j should be small. On the other hand, when we use rotation or amplitude measurements only, then the characteristic length scale of h_j can be larger because the dominant feature of the corresponding kernels is the broad first Fresnel zone. (4) Usually, the gradient of an objective functional with respect to the model parameters (again, see equation 45) is multiplied by a covariance matrix either to yield the direction of steepest ascent or to deliberately smooth the final model. Just as the characteristic length scale of h_j, the correlation length of the covariance matrix

should also be chosen to be smaller for β_a measurements than for measurements of A_v or A_ω, for example.

The choice of the basis functions h_j is of outstanding importance, especially in the framework of linearized inversion (see the Outlook: Possible Setups of Inverse Problems section). In conventional ray-based travel-time tomography, the basis functions must be chosen such that the matrix **A** in equation (42) is nonsingular or at least as well conditioned as possible. The intuitive interpretation of this requirement is that there be a generally good azimuthal ray coverage in the region of interest. Whether suitable basis functions exist in the case of apparent shear-speed measurement, and whether a similar intuitive interpretation exists, still needs further investigations.

In contrast to the β_a kernels, sensitivity densities for rotation amplitude measurements generally reach large absolute values everywhere around the geometric ray path. Their large-scale structure very much resembles the one of sensitivity densities for velocity amplitude measurements. It is, therefore, likely that measurements of A_ω alone may yield similar information on Earth structure as measurements of A_v alone, at least in the context of linearized or gradient method based inversion. It is the combined measurement of A_ω and A_v, that is, the measurement of β_a, which can potentially make a difference.

Throughout the Case Studies section, we limited our attention to the sensitivity of β_a with respect to β. Sensitivity of β_a with respect to the *P*-wave speed, α, is generally small because the velocity amplitudes and rotation amplitudes of *S* body waves and surface waves are only weakly affected by *P*-wave speed variations. The same is true for sensitivity with respect to density.

The natural complement of the apparent *S*-wave speed β_a is the analogously defined apparent *P*-wave speed α_a. Indeed, when $\mathbf{u}(\mathbf{x}, t)$ is a plane *P* wave in a homogeneous, isotropic, and unbounded medium, then $|\dot{\mathbf{u}}|/|s| = |\dot{\mathbf{u}}|/|\nabla \cdot \mathbf{u}| = \alpha$, where α is the *P*-wave speed, and $s = \nabla \cdot \mathbf{u}$. It is, therefore, meaningful to define

$$\alpha_a := A_v A_s^{-1}, \qquad A_s^2 := \int_{-\infty}^{\infty} [F * (Ws)]^2 \, dt \qquad (46)$$

in an arbitrary medium. The subscript *s* in equation (46) refers to the divergence *s* of the displacement field. The analysis of the corresponding sensitivity densities $\delta_\alpha \ln \alpha_a$ is beyond the scope of this article. Still, we remark that the adjoint source for the kernel $\delta_p \ln A_s$ is

$$\mathbf{f}^s(\mathbf{x}, t) = \frac{1}{A_s^2} (\mathfrak{F}s)(\mathbf{x}^r, t)\mathbf{e}_i \frac{\partial}{\partial x_i} \delta(\mathbf{x} - \mathbf{x}^r), \qquad (47)$$

meaning that it is dipolar as is the adjoint source for $\delta_p \ln A_\omega$. We may, therefore, at least hypothesize that $\delta_\alpha \ln \alpha_a$ may also vanish near the source.

Finally, we wish to address the feasibility of a structural inversion using β_a from a purely computational point of view. While such an inversion is clearly more expensive than a travel-time tomography based on the ray method, its computational costs are still moderate, at least compared to full waveform inversion (e.g., Gauthier *et al.*, 1986) or wave equation travel-time inversion (e.g., Luo and Schuster, 1991; Tromp *et al.*, 2005). There are three reasons for this: (1) As already discussed, β_a is sensitive to small-scale structures even when low frequencies are used. Hence, one can choose a broader numerical grid for the computation of the synthetic seismograms. (2) The kernels $\delta_\beta \ln \beta_a$ are small far from the source. It is, therefore, unnecessary to propagate the adjoint wave field all the way back to the source. 3) When lateral variations in the Earth model are small, then one may reduce the computational costs by using a combined-method approach. The forward wave field can be propagated in a 1D model with an inexpensive method until it comes close to the receiver. From there on, a purely numerical method is used that can handle 3D media. The applicability of this approach need to be assessed for each particular 3D Earth model.

Conclusions

This study was motivated by the recent high-quality and consistent observations of rotational ground motions using ring laser technology. The joint processing of rotational and translational motions indicated that information on the subsurface velocity structure might be recoverable even with observations at a single measurement point. This is in contrast to the common requirement in seismology to have access to information from distributed stations (arrays, networks) in order to derive wave-field characteristics such as phase velocities and phase delays relating to subsurface structure.

Our theoretical analysis based upon the adjoint methodology reveals some interesting properties that might one day enable a new type of seismic tomography: (1) Sensitivities of rotational motions alone have very similar shapes to well-known sensitivities of measurements derived from translations (e.g., travel times, amplitudes). (2) The sensitivity of the newly introduced measurement apparent shear-wave speed is essentially based on the difference of sensitivities due to translations and rotations and is highly localized below the receiver position. (3) Because of the specific form of the sensitivity kernels structures well below the analyzed wavelengths might be recoverable, and (4) the concentration of sensitivity close to the receiver might allow the use of efficient hybrid modelling schemes in tomographic inversion schemes.

Our results indicate that additional observations of rotational ground motions are indeed beneficial and may allow estimation of the structure below the receiver on length scales that partly depend on the analyzed frequencies. While in principle, rotational ground motions can be estimated from appropriately sized arrays, and such arrays would offer similar (and additional) information content, it is important to note that array-derived rotations are very sensitive to (1) noise

in the data, (2) variations in coupling properties within the array, (3) nonplanarity of wavefronts, and (4) local structural heterogeneities. In addition, the array size makes the accuracy of the results frequency dependent, and in particular, one would derive rotations with sensors that are contaminated by rotations.

Further studies are necessary to understand the relevance of these concepts in different situations (e.g., local, regional, and global scale, or reservoir conditions) and to develop tomographic inversion schemes based on joint measurements of rotations and translations.

Data and Resources

For the computation of synthetic seismograms and sensitivity kernels we used the high-performance cluster Tethys described by Oeser *et al.* (2006) and the spectral-element code SEC3D described by Fichtner and Igel (2008).

Acknowledgments

References

Aki, K., and P. G. Richards (2002). *Quantitative Seismology*, 2nd Edition, University Science Books.

Aki, K., A. Christoffersson, and E. S. Husebye (1977). Determination of the three-dimensional seismic structure of the lithosphere, *J. Geophys. Res.* **82,** 277–296.

Chavent, G., M. Dupuy, and P. Lemonnier (1975). History matching by use of optimal theory, *J. Soc. Petrol. Eng.* **15,** no. 1, 74–86.

Dahlen, F.A., and A. M. Baig (2002). Fréchet kernels for body-wave amplitudes, *Geophys. J. Int.* **150,** 440–466.

Dahlen, F. A., S.-H. Hung, and G. Nolet (2000). Fréchet kernels for finite-frequency traveltimes—I. Theory, *Geophys. J. Int.* **141,** 157–174.

Ferreira, A. M. G., and H. Igel (2009). Rotational motions of seismic surface waves in a laterally heterogeneous Earth, *Bull. Seismol. Soc. Am.* **99,** no. 2B, 1429–1436.

Fichtner, A., and H. Igel (2008). Efficient numerical surface wave propagation through the optimization of discrete crustal models—A technique based on non-linear dispersion curve matching (DCM), *Geophys. J. Int.* **173,** no. 2, 519–533.

Fichtner, A., H.-P. Bunge, and H. Igel (2006). The adjoint method in seismology—I. Theory, *Phys. Earth Planet. Int.* **157,** 86–104.

Gauthier, O., J. Virieux, and A. Tarantola (1986). Two-dimensional non-linear inversion of seismic waveforms: Numerical results, *Geophysics* **51,** no. 7, 1387–1403.

Graizer, V. M. (2005). Effect of tilt on strong motion data processing, *Soil Dyn. Earthq. Eng.* **25,** 197–204.

Igel, H., A. Cochard, J. Wassermann, A. Flaws, U. Schreiber, A. Velikoseltsev, and N. Pham Dinh (2007). Broad-band observations of earthquake-induced rotational ground motions, *Geophys. J. Int.* **168,** no. 1, 182–197.

Igel, H., U. Schreiber, A. Flaws, B. Schuberth, A. Velikoseltsev, and A. Cochard (2005). Rotational motions induced by the *M* 8.1 Tokachi-oki earthquake, September 25, 2003, *Geophys. Res. Lett.* **32,** L08309.

Kennett, B. L. N., E. R. Engdahl, and R. Buland (1995). Constraints on seismic velocities in the Earth from traveltimes, *Geophys. J. Int.* **122,** 108–124.

Lay, T., and T. C. Wallace (1995). *Modern Global Seismology*, Academic Press, New York.

Lions, J. L. (1968). *Contrôle optimal de systèmes gouvernés par des équations aux dérivées partielles*, Dunod Gauthier-Villars.

Luo, Y., and G. T. Schuster (1991). Wave equation traveltime inversion, *Geophysics* **56,** no. 5, 645–653.

Marquering, H., F. A. Dahlen, and G. Nolet (1999). Three-dimensional sensitivity kernels for finite-frequency traveltimes: The banana-doughnut paradox, *Geophys. J. Int.* **137,** 805–815.

Nigbor, R. L. (1994). Six-degree-of-freedom ground-motion measurement, *Bull. Seismol. Soc. Am.* **84,** no. 5, 1665–1669.

Nolet, G. (1993). Solving large linearized tomographic problems, in *Seismic Tomography*, K. Iyer and H. M. Hirahara (Editors), Chapman and Hall, London.

Oeser, J., H.-P. Bunge, and M. Mohr (2006). Cluster design in the Earth sciences: Tethys, *Proc. of High Performance Computing and Communications* **4208,** 31–40.

Pancha, A., T. H. Webb, G. E. Stedman, D. P. McLeod, and K. U. Scheiber (2000). Ring laser detection of rotations from teleseismic waves, *Geophys. Res. Lett.* **27,** no. 21, 3553–3556.

Pillet, R., and J. Virieux (2007). The effects of seismic rotations on inertial sensors, *Geophys. J. Int.* **171,** no. 3, 1314–1323.

Schreiber, U., G. E. Stedman, H. Igel, and A. Flaws (2006). Ring laser gyroscopes as rotation sensors for seismic wave studies, in *Earthquake Source Asymmetry, Structural Media and Rotation Effects* R. Teisseyre, M. Takeo, and E. Majewski (Editors), Springer-Verlag, New York.

Sieminski, A., H. Paulssen, J. Trampert, and J. Tromp (2008). Finite-frequency SKS splitting: Measurement and sensitivity kernels, *Bull. Seismol. Soc. Am.* **98,** no. 4, 1797–1810.

Suryanto, W. (2006). *Rotational Motions in Seismology: Theory and Application*, *Dissertation*, Faculty of Earth Sciences, Ludwig-Maximilan University, München, Germany.

Takeo, M. (1998). Ground rotational motions recorded in near-source region of earthquakes, *Geophys. Res. Lett.* **25,** 789–792.

Tarantola, A. (1988). Theoretical background for the inversion of seismic waveforms, including elasticity and attenuation, *Pure Appl. Geophys.* **128,** 365–399.

Trifunac, M. D., and M. I. Todorovska (2001). A note on the usable dynamic range of accelerographs recording translation, *Soil Dyn. Earthq. Eng.* **21,** no. 4, 275–286.

Tromp, J., C. Tape, and Q. Liu (2005). Seismic tomography, adjoint methods, time reversal, and banana-donut kernels, *Geophys. J. Int.* **160,** 195–216.

Yomogida, K. (1992). Fresnel zone inversion for lateral heterogeneities in the Earth, *Pure Appl. Geophys.* **138,** no. 3, 391–406.

Ludwig-Maximilian University
Department of Earth and Environmental Sciences
Theresienstrasse 41
80339 Munich, Germany